

---

# Vision Transformer Visualization: What Neurons Tell and How Neurons Behave?

---

**Van-Anh Nguyen\***

Monash University, Australia  
van-anh.nguyen@monash.edu

**Khanh Pham Dinh\***

OrientSoftware  
khanh.pham@orientsoftware.com

**Long Tung Vuong**

Monash University, Australia  
longvt94@gmail.com

**Thanh-Toan Do**

Monash University, Australia  
toan.do@monash.edu

**Quan Hung Tran**

Adobe Research, San Jose, CA, USA  
qtran@adobe.com

**Dinh Phung**

Monash University, Australia  
dinh.phung@monash.edu

**Trung Le**

Monash University, Australia  
trunglm@monash.edu

## Abstract

Recently vision transformers (ViT) have been applied successfully for various tasks in computer vision. However, important questions such as why they work or how they behave still remain largely unknown. In this paper, we propose an effective visualization technique, assisting us in exposing the information carried in neurons and feature embeddings across the ViT's layers. Our approach departs from the computational process of ViTs with a focus on visualizing the local and global information in input images and the latent feature embeddings at multiple levels. Visualizations at the input and embeddings at level 0 reveal interesting findings such as providing support as to why ViTs are rather generally robust to image occlusions and patch shuffling; or unlike CNNs, level 0 embeddings already carry rich semantic details. Next, we develop rigorous framework to perform effective visualizations across layers, exposing the effects of ViTs filters and grouping/clustering behaviors to object patches. Finally, we provide comprehensive experiments on real datasets to qualitatively and quantitatively demonstrate the merit of our proposed methods as well as our findings. [https://github.com/byM1902/ViT\\_visualization](https://github.com/byM1902/ViT_visualization)

## 1 Introduction

Inspired by the success of Transformer [28] in natural language processing [8], Vision Transformers (ViT) [9, 25] have been proposed for vision data with a specific focus on large-scale and complex datasets such as ImageNet [7, 20]. Subsequently, inherited from the original ViT [9], many variants of ViTs have been explored to deal with various applications in computer vision ranging from image classification [25, 4], object detection [3, 32, 14], semantic segmentation [31, 23, 29], image captioning [6, 30] to name a few.

---

\*The first two authors contributed equally to this work

With the engagement of the multi-head self-attention mechanism [28], ViTs operating principle is fundamentally different from that of Convolutional Neural Networks (CNN) [13, 11]. Therefore, it is essential to answer the questions regarding the intriguing properties of ViTs. For instance, "*how are ViTs fundamentally different from CNNs?*", "*what are the intriguing properties of ViTs?*", or "*how are ViTs robust to adversarial attacks, image occlusions, or patch shuffling?*". Targeting these questions, some works have been dedicated to studying the characteristics and behaviors of ViT, notably [17, 2, 22, 19, 18].

Particularly, Naseer et al. [17] studied the intriguing properties of ViTs and found that ViTs are more robust to image occlusions, patch shuffling, and shape-biased learning than CNNs. Shao et al. [22] analyzed ViTs against adversarial noise and demonstrated that ViTs are more robust to high frequency changes. Additionally, Bhojanapalli et al. [2] studied ViTs against spatial perturbations [22] and showed their robustness to the removal of almost any single layer and their robustness superiority to the ResNet counterparts. Recently, to compare the robustness of ViTs and CNNs, Yutong et al. [1] undertook comprehensive and fair experiments to come with a quite opposite conclusion: ViTs are not actually more robust than CNNs w.r.t. adversarial examples. Furthermore, Maithra et al. [19] analyzed the internal representation structure of ViTs and CNNs on image classification benchmarks and found that ViTs have more uniform representations across all layers. Namuk et al. [18] studied the behavior of multi-head self-attentions (MSA) and convolutional layers (Convs), and then proposed to replace Conv blocks at the end of a stage with MSA blocks for improving the performance.

In this paper, to enrich the understanding of the behaviors and characteristics of ViTs, we propose a visualization technique that allows us to visualize the information in input images captured in neurons and feature embeddings across the layers of ViTs. Furthermore, by observing and analyzing the outputs of our visualization technique, we observe an interesting clustering behavior of feature embeddings across the layers for which we can develop a simplified mathematical explanation. More concretely, our contributions in this paper can be summarized:

- We propose a visualization technique to visually expose the local/global information in input images carried in neurons and embeddings across the layers of ViTs. Additionally, using the proposed visualization technique, we can partly explain why ViTs are rather robust to image occlusions and patch shuffling.
- Moreover, by visualizing neurons and embeddings at the layer 0, we find that the filters of ViTs (i.e.,  $16 \times 16$  filters) are sufficiently powerful to activate multiple object types across multiple images. This is different from CNNs, where the low-level filters are typically small and can capture only low-level features (e.g., edges or lines) at low-level layers.
- Furthermore, by analyzing the outputs of our visualization technique, we further realize the clustering behavior of feature embeddings across layers. Specifically, when moving up to higher layers, ViT's feature embeddings at each layer tend to form more well-separated clusters, each of which is dominated by feature embeddings corresponding to the same object type's patches (e.g., feature embeddings of the dog patches); the attention weights for feature embeddings in an object cluster are also higher than others. Finally, we develop a simplified mathematical theory to explain this clustering behavior and conduct experiments on the Pascal VOC 2009 dataset [10] to quantitatively verify it.

## 2 Vision Transformers

We recap the technical specification of ViT [9], which lays foundation for the presentation of our visualization technique in the sequel. Given an image  $\mathbf{x} \in \mathbb{R}^{H \times W \times C}$ , we divide this image to  $N$  patches  $[\mathbf{x}_p^i]_{i=1}^N$ , each of which has the shape  $\mathbf{x}_p^i \in \mathbb{R}^{P \times P \times C}$  with  $N = \frac{H \times W}{P^2}$ . We next apply  $D$  filters with the shape  $P \times P \times C$  to each patch to work out a patch embedding  $\tilde{\mathbf{z}}_0^i \in \mathbb{R}^{D \times 1}$  ( $i = 1, \dots, N$ ). We then concatenate the patch embedding with the class embedding  $\mathbf{x}_{class} = \tilde{\mathbf{z}}_0^0$ . Finally, we add the position encoding  $\mathbf{E}_{pos} \in \mathbb{R}^{(N+1) \times D}$  to obtain the patch embeddings and class embedding at the layer 0 as

$$\mathbf{z}_0 = [\mathbf{x}_{class}, \tilde{\mathbf{z}}_0^1, \dots, \tilde{\mathbf{z}}_0^N]^T + \mathbf{E}_{pos} \in \mathbb{R}^{(N+1) \times D}.$$

The representations at layer 0 are fed to the Transformer encoder [27] consisting of alternating layers of multi-headed self-attention (MSA) and MLP blocks. Layer norm (LN) is applied before every

block, and residual connections after every block. Additionally, the MLP contains two layers with a GELU non-linearity.

$$\begin{aligned}\tilde{\mathbf{z}}_l &= \text{MSA}(\text{LN}(\mathbf{z}_{l-1})) + \mathbf{z}_{l-1}, \quad l = 1, \dots, L \\ \mathbf{z}_l &= \text{MLP}(\text{LN}(\tilde{\mathbf{z}}_l)) + \tilde{\mathbf{z}}_l, \quad l = 1, \dots, L \\ \mathbf{y} &= \text{LN}(\mathbf{z}_L^0).\end{aligned}$$

Here we note that we use the pretrained ViT [9] for the visualization and empirical studies of the behaviors of ViT. Therefore, we have  $H = W = 224$ ,  $D = 768$ , and  $N = 14 \times 14 = 196$ .

### 3 Visualization for ViT

In this section, we first present our visualization technique for neurons and embeddings across the layer 0 and subsequent layers. We then discuss the findings based on the observation of the visual outputs. Interestingly, the visual outputs give us a hint on the clustering behavior of the patch embeddings corresponding to the objects in an input image. We finally conduct further experiments on real images to quantitatively confirm this finding.

#### 3.1 What Do Neurons Tell?

##### 3.1.1 Visualization for Layer 0

We visualize to answer the question: “*What information is captured or represented by a neuron or an embedding at the layer 0?*”. Since we convolve a *specific filter* with an *image patch* to compute a neuron at the layer 0 and *all D filters* with an *image patch* to form a patch embedding, a neuron or patch embedding at the layer 0 can only capture a local information of a patch.

**Visualizing a neuron and an embedding at the layer 0:** The neuron  $\mathbf{z}_0^{i,j}$  (i.e., the neuron  $j$  of the patch embedding  $i$ ) is formed by convolving the filter  $\mathbf{f}_j \in \mathbb{R}^{P \times P \times C}$  ( $1 \leq j \leq D$ ) and the patch  $\mathbf{x}_p^i$ . Therefore, this neuron contains a local information of the patch  $i$  w.r.t. the filter  $\mathbf{f}_j$ , meaning that it captures local information from a view of a patch. To visualize the neuron  $\mathbf{z}_0^{i,j}$ , we perform the element-wise product between the patch and the filter:  $\mathcal{V}(\mathbf{z}_0^{i,j}) = \mathbf{f}_j \otimes \mathbf{x}_p^i \in \mathbb{R}^{P \times P \times C}$ . Here we denote  $\mathcal{V}(\mathbf{z}_0^{i,j})$  as the *visualization of the neuron*  $\mathbf{z}_0^{i,j}$ . Furthermore, to visualize the patch embedding  $\mathbf{z}_0^i$  (i.e., the row  $\mathbf{z}_0^{i,1:D}$ ), we overlay the visualizations  $\mathcal{V}(\mathbf{z}_0^{i,1:D})$ . In other words, we stack the  $D$  tensors/images  $\mathcal{V}(\mathbf{z}_0^{i,j}) \in \mathbb{R}^{P \times P \times C}$  to represent the information of the patch embedding  $\mathbf{z}_0^i$ . Obviously, the visualization  $\mathcal{R}(\mathbf{z}_0^i)$  of  $\mathbf{z}_0^i$  can only capture a local information according to a multi-view of the patch  $\mathbf{x}_p^i$ .

Moreover, we visualize all neurons in the column  $j$  corresponding to the filter  $\mathbf{f}_j$  (i.e., the column  $\mathbf{z}_0^{1:N,j}$ ) by placing  $\mathcal{V}(\mathbf{z}_0^{1:N,j})$  in the shape of input image. This can be realized by simply moving the filter  $\mathbf{f}_j$  across all patches and doing the element-wise products on the fly. Certainly, the visualization  $\mathcal{R}(\mathbf{z}_0^{1:N,j})$  can capture a global information of an entire image w.r.t. a view or a filter. Our visualization for the layer 0 is summarized in Figure 1.

**Visualization of a specific neuron and an embedding on the layer 0:** We now visualize *the neurons on the patch embedding 1* in Figure 2. Each neuron contains a local information of the image patch 1 or a view of this image patch. Moreover, we overlay the visualizations of 768 neurons in the row 1 together to yield the visualization of the 768-dimensional patch embedding.

**Visualization of a column of neurons corresponding to a filter on the layer 0:** We choose some filters and visualize the neurons corresponding to these filters on the layer 0 in Figure 3. The neurons corresponding to a filter can be represented by an image formed by convolving this filter and the input image. In other words, these neurons represent a single-view of the entire image. We observe that a  $16 \times 16 \times 3$  filter of ViT is sufficiently powerful, hence it can be learned to optimize and emphasize many object types across various images. For instance, the filter 714 can activate various elephants with different sizes, fishes, and etc. This makes sense because the large  $16 \times 16 \times 3$  filters of ViT make a strong optimization problem with  $16 \times 16 \times 3$  variables to optimize on various object types

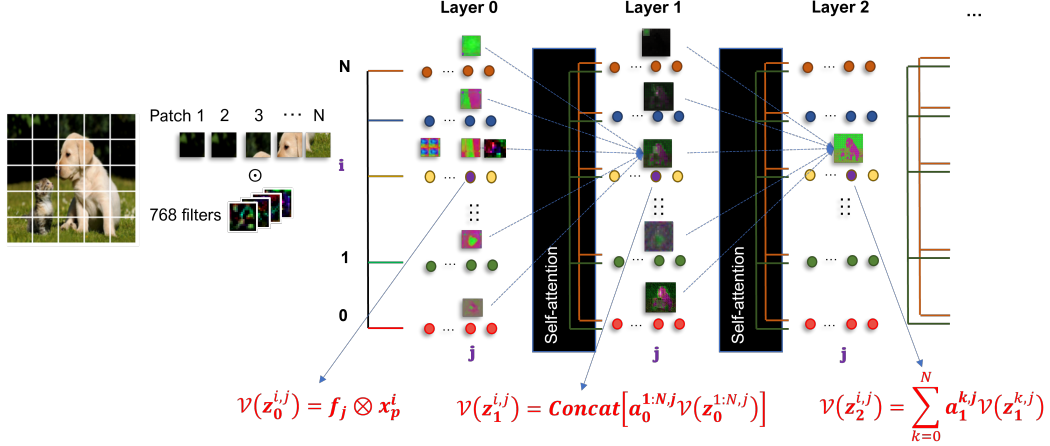


Figure 1: Overview of our visualization technique. At the layer 0, the visualization of the neuron  $\mathbf{z}_0^{i,j}$  is  $\mathcal{V}(\mathbf{z}_0^{i,j}) = \mathbf{f}_j \otimes \mathbf{x}_p^i \in \mathbb{R}^{P \times P \times C}$ . At the layer 1, we arrange  $\mathbf{a}_0^{k,i} \mathcal{V}(\mathbf{z}_0^{k,j}) \in \mathbb{R}^{P \times P \times C}$ ,  $k = 1, \dots, N$  to form an image for  $\mathcal{V}(\mathbf{z}_1^{i,j}) = \text{Concat}[\mathbf{a}_0^{1:N,i} \mathcal{V}(\mathbf{z}_0^{1:N,j})]$ . At the layer 2, we employ  $\mathcal{V}(\mathbf{z}_2^{i,j}) = \sum_{k=0}^N \mathbf{a}_1^{k,i} \mathcal{V}(\mathbf{z}_1^{k,j})$ .

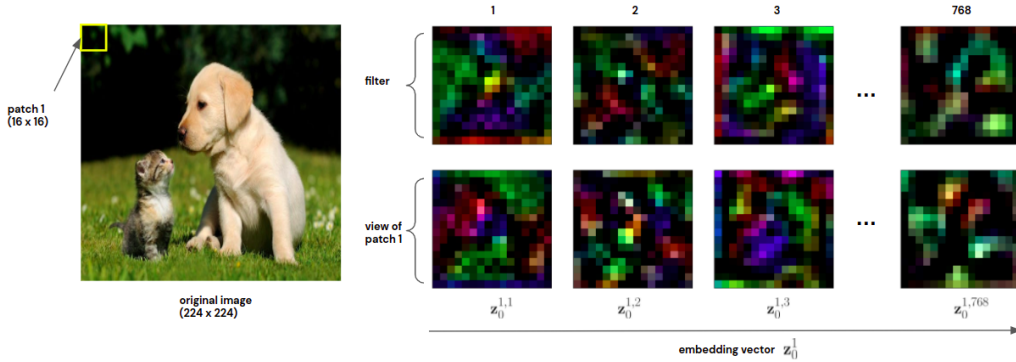


Figure 2: Visualization of the neurons and the patch embedding 1 on the layer 0.

across images. It is worth noting that for state-of-the-art CNNs [11, 24], much smaller  $3 \times 3 \times 3$  or  $5 \times 5 \times 3$  filters are employed, hence the low-level filters can only learn low-level features such as vertical/horizontal lines or edges, whereas the higher-level filters can combine low-level features to obtain more abstract features. We further observe that the filters are complementary in the sense that each of them is responsible for a set of object types. For instance, although the filter 714 cannot activate the dog or cat objects, the filter 732 can complement it to activate these object types.

### 3.1.2 Visualization for Subsequent Layers

**Visualization for Layer 1:** We answer the same question but for the neurons and embeddings on the subsequent layers. We start with the layer 1. The neuron  $\mathbf{z}_1^{i,j}$  is computed based on the neurons  $\mathbf{z}_0^{0:N,j}$  on the previous layer. Each  $\mathbf{z}_0^{i,j}$  represents the view  $j$  of the patch  $i$ , hence the neuron  $\mathbf{z}_1^{i,j}$  combining  $\mathbf{z}_0^{0:N,j}$  contains a global information of an entire image. Our purpose is to visualize the information in an input image captured in a neuron at a layer. Therefore, for the sake of visualization, we mainly focus on the multi-head self-attention and consider how to visualize the information of  $\mathcal{V}(\mathbf{z}_1^{i,j})$  based on  $\mathcal{V}(\mathbf{z}_0^{0:N,j})$  and the attention weights  $\mathbf{a}_0^{0:N,j}$ , where  $\mathbf{a}_0^{k,j}$  represents the attention weight of the embeddings  $\mathbf{z}_0^k$  and  $\mathbf{z}_0^j$ . Visualization at this layer is summarized in Figure 1.

Because the neuron  $\mathbf{z}_1^{i,j}$  contains a global information of an entire image and computationally depends on  $\mathbf{z}_0^{0:N,j}$  and the attention weights  $\mathbf{a}_0^{0:N,j}$  via a self-attention, we visualize  $\mathcal{V}(\mathbf{z}_1^{i,j})$  by arranging

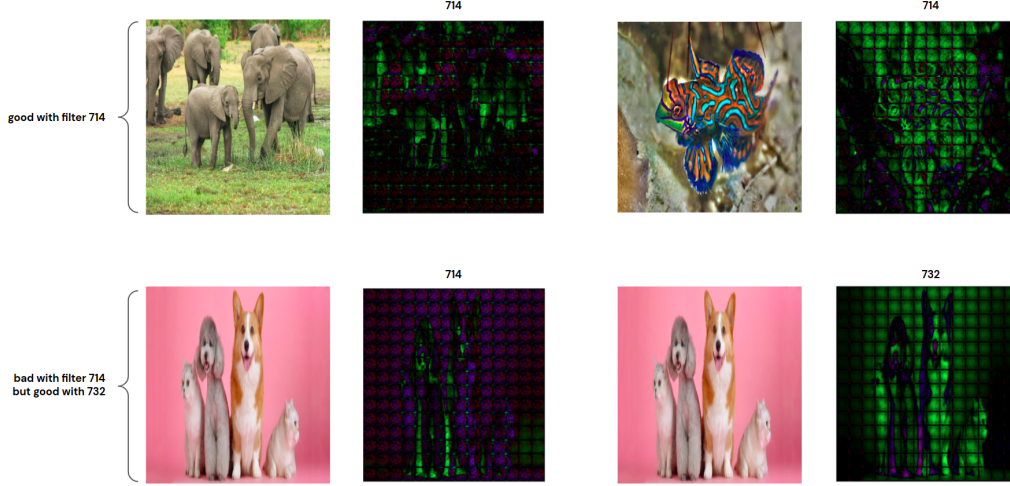


Figure 3: Visualization of the neurons in the columns  $\mathbf{z}_0^{1:N,714}$  corresponding to the filter 714 and  $\mathbf{z}_0^{1:N,732}$  corresponding to the filter 732 for some input images. The filter 714 is good to activate elephants and fishes, whereas the filter 732 is good to activate dogs and cats.

$\mathbf{a}_0^{k,i} \mathcal{V}(\mathbf{z}_0^{k,j}) \in \mathbb{R}^{P \times P \times C}$ ,  $k = 1, \dots, N$  to form an image or a tensor  $\mathcal{V}(\mathbf{z}_1^{i,j}) \in \mathbb{R}^{H \times W \times C}$  in the order according to  $k$ . By doing so, we can summarize the information of  $\mathcal{V}(\mathbf{z}_0^{k,j})$  with the attention level  $\mathbf{a}_0^{k,j}$  for  $k = 1, \dots, N$  into  $\mathcal{V}(\mathbf{z}_1^{i,j})$ . Additionally, to take into account multiple heads, we use the average of the attention weights across the heads for our visualization. Moreover, we do not use the information from  $\mathbf{z}_0^{0,j}$  in the class embedding when visualizing  $\mathbf{z}_1^{i,j}$  since it does not relate directly to a patch. Finally, to yield the visualization  $\mathcal{V}(\mathbf{z}_1^i) = \mathcal{V}(\mathbf{z}_1^{i,1:D})$  for the embedding  $i$  at the layer 1, we simply stack  $\mathcal{V}(\mathbf{z}_1^{i,1:D})$ .

**Visualization for Layer  $\geq 2$ :** We present how to visualize the neurons and embeddings on the layer 2 based on those on the layer 1. We apply the same way to visualize for the remaining layers. Recap that each neuron  $\mathbf{z}_1^{i,j}$  on the layer 1 contains a global information of an entire image. Because  $\mathbf{z}_2^{i,j}$  computationally depends on the neurons  $\mathbf{z}_1^{0:N,j}$  with the attention weights  $\mathbf{a}_1^{0:N,j}$ , we obtain the visualization  $\mathcal{V}(\mathbf{z}_2^{i,j})$  for the neuron  $\mathbf{z}_2^{i,j}$  by  $\mathcal{V}(\mathbf{z}_2^i) = \sum_{k=0}^N \mathbf{a}_1^{k,i} \mathcal{V}(\mathbf{z}_1^{k,j})$ , which returns an image or a tensor with the shape  $\mathbb{R}^{H \times W \times C}$ , meaning that the neuron  $\mathbf{z}_2^{i,j}$  contains a global information of an entire image. Visualization at this layer is summarized in Figure 1.

**Visualization of neurons and embeddings across layers:** In Figure 4, we visualize the neurons corresponding to the filter 3 across the layers for some cases: (i) the neuron relevant to the class embedding, (ii) the neuron relevant to a background (non-object) patch, and (iii) the neuron relevant to a foreground (object) patch. We have the following observations in order. *First*, the neuron on the class embedding at high layers contain sufficient information of the objects for making predictions. This is possibly due to the fact that we make predictions on the class embedding directly. *Second*, the neurons corresponding to the patches 62 and 78 (i.e., two patches on the dog object) contain a clear information of the dog object, which is strengthened at higher layers. *Third*, the neuron on the background patch also contains the information of the objects due to the self-attentions, but the information amount are less than the neurons on the foreground patches. *Fourth*, the positional encoding information is retained in the neurons. *Fifth*, the visualizations of the neurons belonging to the same object (e.g., the patches 62 and 78 for the dog object) are more similar to those in other objects or background. This hints us about the *clustering behavior of the embeddings* corresponding to the foreground patches of the same object, leading to our further investigation in Section 3.2.

**Visualization of the information retained with an occlusion:** Inspired by [17], we visualize the information from an input image retained in a neuron at a certain layer with an occlusion. We examine three cases: (i) *Random drop*, (ii) *Non-salient drop*, and (iii) *Salient drop*. For the random

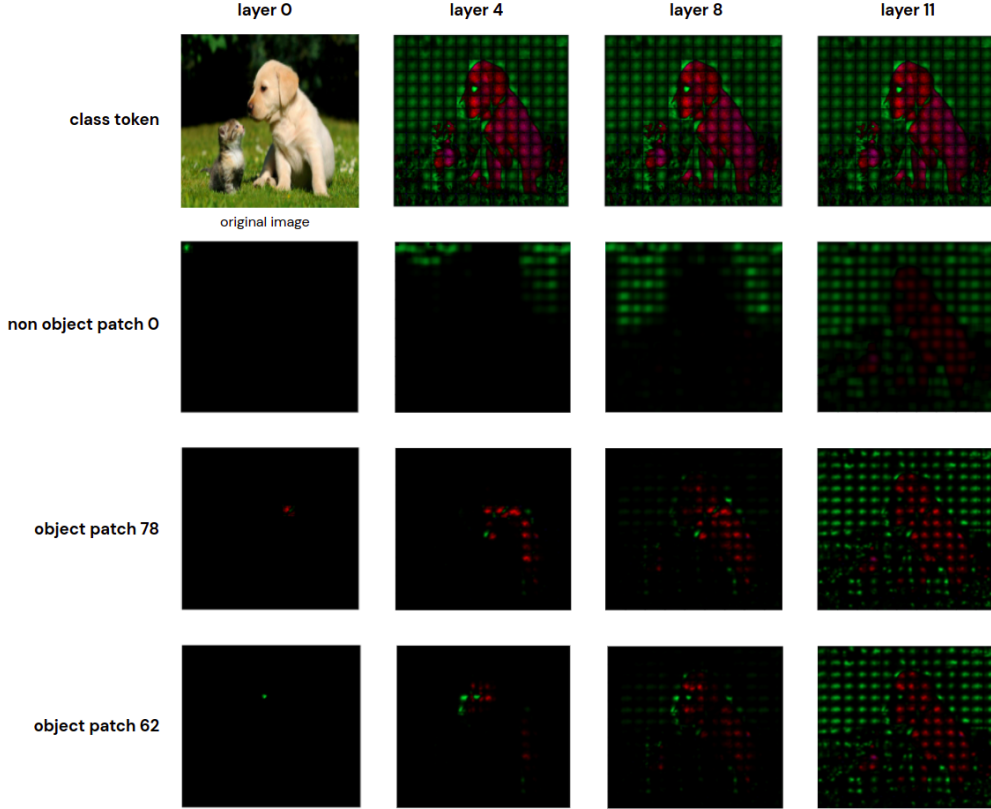


Figure 4: Visualization of the neurons corresponding to background (none-object) and foreground (object) patches.

drop, because the patches are randomly dropped, the object information is partly retained rather well. Additionally, the information from the dropped patches seems hard to be recovered in the higher layers, which hurts the final prediction. For the salient drop, the object information retained a little, whereas for the non-salient drop, the object information is remained rather intact. These concur with the observations in [17].

### 3.2 How Do Neurons Behave?

As hinted by our clustering behavior conjecture in the previous section, we quantitatively and qualitatively investigate this behavior on real images. To realize this clustering behavior, we apply t-SNE [26] to visualize the high-dimensional patch embeddings across the layers.

**t-SNE visualization of the embeddings across the layers:** We use t-SNE [26] to visualize the patch embeddings at each layer of ViT for input images in Figure 6. Particularly, in Figure 6a, we visualize the patch embeddings for a single image with a dog object and a cat object at the layers 0, 6, and 11. It can be observed that when moving up to higher layers, the *cluster for the dog patch embeddings* (i.e., the green points) becomes more separated with the *cluster for the cat patch embeddings* (i.e., the orange points). In Figure 6b, we concatenate four images to have an input image with diverge objects and then visualize the embeddings at the layers 0, 6, and 11. Again, we observe the same clustering behavior, i.e., the clusters for the object embeddings become more separated at higher layers. In addition, at the last layer, we visualize the *attention weights w.r.t. the class token* for patch embeddings with a bigger size and a brighter color for a higher value. It can be seen that the object-patch embeddings have higher attention weights

In what follows, we provide a sketch mathematical explanation for the clustering behavior. According to our analysis, this exciting behavior mainly comes from the nature of the self-attention mechanism,

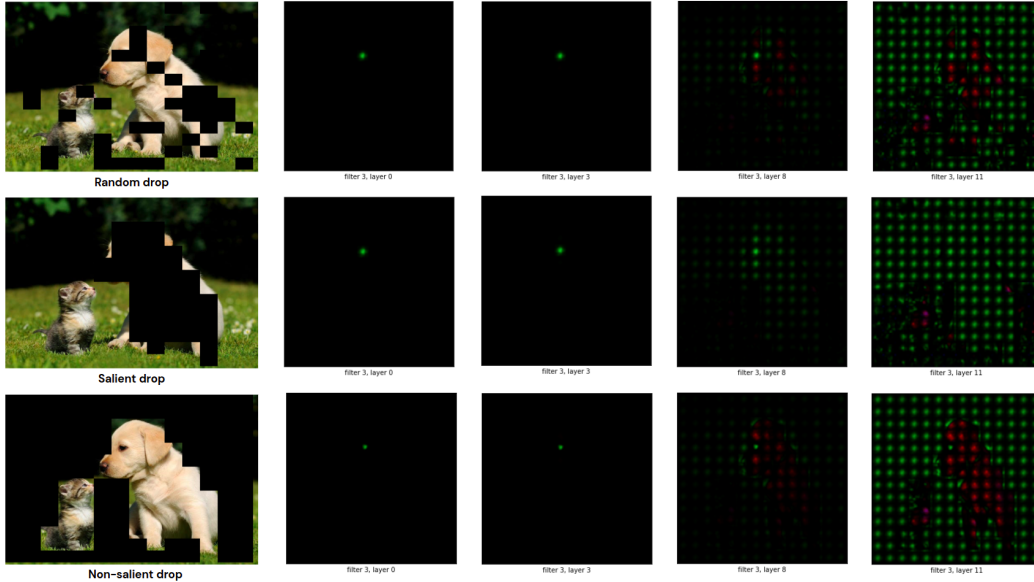


Figure 5: Visualization of the information retained with an occlusion. Information retained a little with the salient drop, retained more with the random drop, and remained rather intact with the non-salient drop.

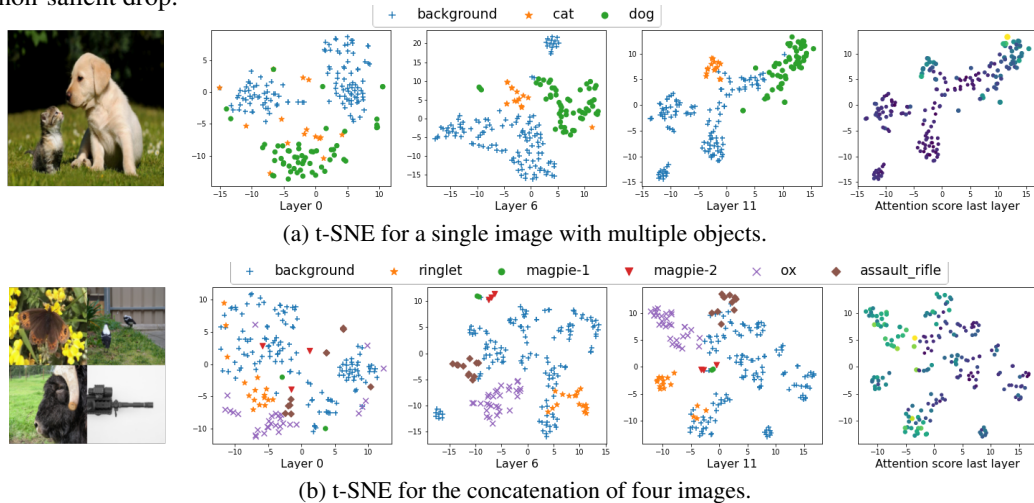


Figure 6: t-SNE of feature embeddings across the layers of ViT. At higher layers, the object-patch embeddings form more separated clusters. Meanwhile, the attention weights w.r.t. the class token of object-patch embeddings are higher than others.

which makes two similar embeddings to become even more similar. To simplify the context, we only consider the single-head self-attention case.

**Mathematical explanation for the clustering behavior:** We consider the single-head self-attention with the key matrix  $W_K$ , the query matrix  $W_Q$ , and the value matrix  $W_V$ . We examine the embeddings at two consecutive layers:  $\mathbf{z}_t \in \mathbb{R}^{(N+1) \times D}$  and  $\mathbf{z}_{t+1} \in \mathbb{R}^{(N+1) \times D}$ , where each row of them is an embedding. The attention weights  $\mathbf{a}_t^{k,j}$  are computed based on the similarity of the linear projections of  $\mathbf{z}_t^k$  and  $\mathbf{z}_t^j$  w.r.t.  $W_K$  and  $W_Q$  respectively. We then apply the linear projection to  $\mathbf{z}_t^j$ ,  $j = 0, \dots, N$ , then compute  $\tilde{\mathbf{z}}_{t+1}^j$ ,  $j = 0, \dots, N$ , and finally do another linear projection to project  $\tilde{\mathbf{z}}_{t+1}^j$ ,  $j = 0, \dots, N$  back to the embedding space to obtain  $\mathbf{z}_{t+1}^j$ ,  $j = 0, \dots, N$ . To simplify our analysis, we further assume that  $W_V = \mathbb{I}$  (i.e., the identity matrix). Therefore, we compute the embeddings in the next layer as  $\mathbf{z}_{t+1}^j = \sum_{k=0}^N \mathbf{a}_t^{k,j} \mathbf{z}_t^k$ . We develop the following theorem regarding the clustering behavior of the embeddings.

**Theorem 3.1.** (Proof can be found in the supplementary material) Let  $d(A) = \max_{\mathbf{a}, \mathbf{b} \in A} \|\mathbf{a} - \mathbf{b}\|_2$  be the diameter of the set  $A$ . The following statements hold

i)  $d(Z_{t+1}) \leq d(Z_t)$ , where  $Z_t$  and  $Z_{t+1}$  are the sets of the row vectors (i.e., the embeddings) of  $\mathbf{z}_t$  and  $\mathbf{z}_{t+1}$  respectively.

ii) Assume that the embeddings  $Z_t$  (or  $\mathbf{z}_t$ ) can be grouped into  $M$  clusters  $Z_t^m = \{\mathbf{z}_t^j : j \in G^m\}$ , where  $\{G^m\}_{m=1}^M$  is a partition of  $\{0, 1, \dots, N\}$  such that if  $j \in G^m$  and  $j' \in G^{m'}$  with  $m \neq m'$ , the attention weight  $\epsilon_l < \mathbf{a}_t^{j',j} < \epsilon_u$  for  $\epsilon_u \geq \epsilon_l \geq 0$ . This condition means that if  $\mathbf{z}_t^j$  and  $\mathbf{z}_t^{j'}$  belong to two different clusters, they are less similar and their attention weight  $\mathbf{a}_t^{j',j}$  is possibly small. Let  $N_m = |G^m|$  be the cardinality of the cluster  $m$ . For any  $m$ , we have the following inequality:

$$d(Z_{t+1}^m) < (1 - A_m \epsilon_l)^2 d(Z_t^m) + A_m \epsilon_u d(Z_t) [A_m \epsilon_u d(Z_t) + 2], \quad (1)$$

where  $A_m = N + 1 - N_m$  and  $Z_{t+1}^m = \{\mathbf{z}_{t+1}^i : i \in G^m\}$  is the cluster in the next layer. Note that  $d(Z_{t+1}^m)$  and  $d(Z_t^m)$  are exactly the intra-cluster distances for these clusters.

Theorem 3.1 asymptotically explains the clustering behavior. First, Theorem 3.1i discloses that the diameter of the set of the next embeddings gets smaller. Second, Theorem 3.1ii states that if the clusters become gradually well-separated,  $\epsilon_u \geq \epsilon_l$  gets smaller and approaches 0, asymptotically meaning that  $d(Z_{t+1}^m) \leq d(Z_t^m)$ , hence the intra-distance of a cluster gets decreased at the next layer. We notice that because the object patches of the same object are possibly similar, their embeddings at the layer 0 are more similar. Therefore, we possibly depart with quite good clusters. However, the difference among embeddings are tiny due to initial values for the weight matrices. We next experiment on real images to quantitatively verify the clustering behavior.

**Quantitative verification of the clustering behavior:** We experiment on the real images from the Pascal VOC 2009 dataset [10]. We select the 500 images and use the ground-truth pixel label to label an object type or a background for a image patch. Additionally, we notice that objects in the ImageNet dataset often take a big area in images, hence to assign an object label for an image patch, this patch needs to be overlapped at least 40% with the object. Using this criterion, we select images with at least two objects, wherein each object has at least 3 patches validly belonging to it.

For each selected image, we feed to the ViT to extract the embeddings at the layers. We employ the DBSCAN clustering algorithm [15] to cluster the embeddings at each layer. For the clustering solution at each layer, we measure the purity score [16], the Silhouette score [21], the average cosine similarity of the embeddings in a cluster, the average cosine similarity of the embeddings relevant to an object, and the unique label ratio (cf. the supplementary material for the formula of the clustering measures).

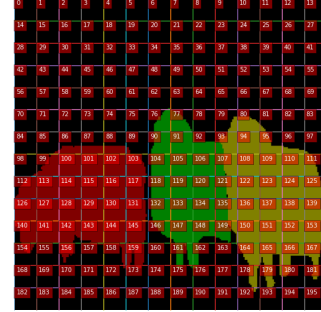


Figure 7: How to label patches with object type labels or background.

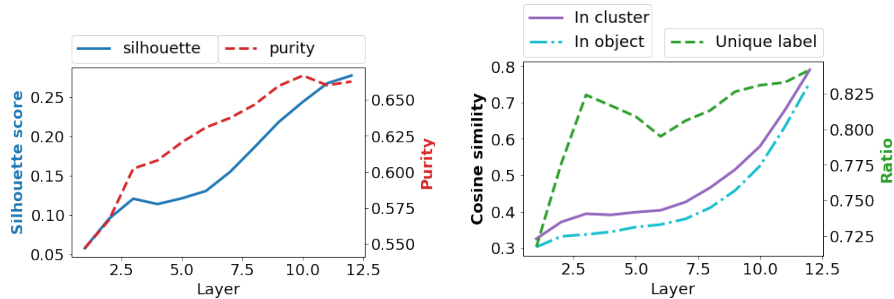
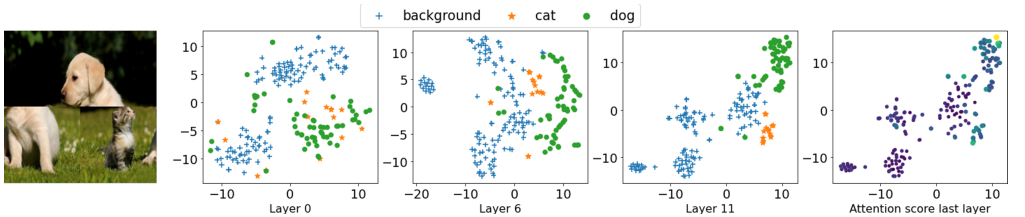


Figure 8: The visualization of the average the clustering measures on the Pascal VOC dataset across the ViT’s layers. Left: the purity and Silhouette scores. Right: the average cosine similarity of the embeddings in a cluster, the average cosine similarity in of the embeddings relevant to an object, and the unique label ratio. At higher layers, we obtain more pure object-dominated clusters with high similar object-patch embeddings.

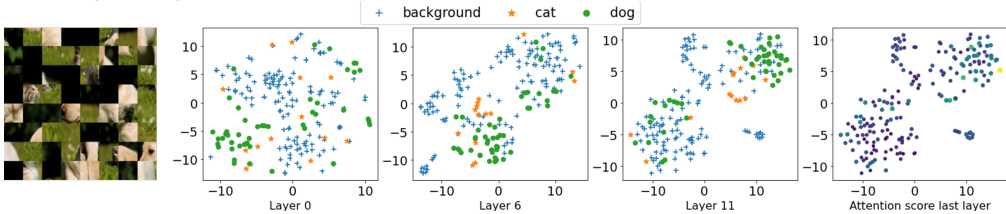
A *high purity* means that each cluster is pure, meaning that there exists a particular object or background so that its patches really dominate this cluster. A *high Silhouette* score implies the intra-cluster distances are relatively smaller than the inter-cluster distances. A *high average cosine*

*similarity of the embeddings* in a cluster means that the embeddings in a cluster are highly similar, whereas a *high average cosine similarity of the embeddings relevant to an object* means that the embeddings corresponding to object patches are highly similar. Finally, the unique label ratio is computed as the ratio of the number of unique cluster labels (i.e., the cluster label is the object or background patches dominating the cluster) and the number of labels (i.e., the number of objects plus 1), hence a *high unique label rate* implies that there are more object-dominated clusters.

Figure 8 visualizes the clustering measures across the layers on the Pascal VOC dataset. It can be observed that the purity becomes increased at higher layers, indicating purer clusters. The Silhouette score gets increased, indicating the intra-cluster distances decrease faster than the inter-cluster distances when moving to higher layers. The average cosine similarity of the embeddings in a cluster gets increased, indicating the embeddings in a cluster becomes more similar at higher layers. The average cosine similarity of the embeddings relevant to an object gets increased, indicating the embeddings of object patches becomes more similar at higher layers. The unique label ratio gets increased, indicating more object-dominated clusters at higher layers. Putting altogether, at higher layers, we obtain more pure object-dominated clusters with high similar object-patch embeddings, concurring with the clustering behavior.



(a) Image shuffled with the grid  $2 \times 2$ . The object embeddings form clusters and attention weights for object embeddings are high.



(b) Image shuffled with the grid  $8 \times 8$ . The object embeddings do not form clusters and attention weights for object embeddings are still high.

Figure 9: t-SNE of feature embeddings across the layers for shuffling images.

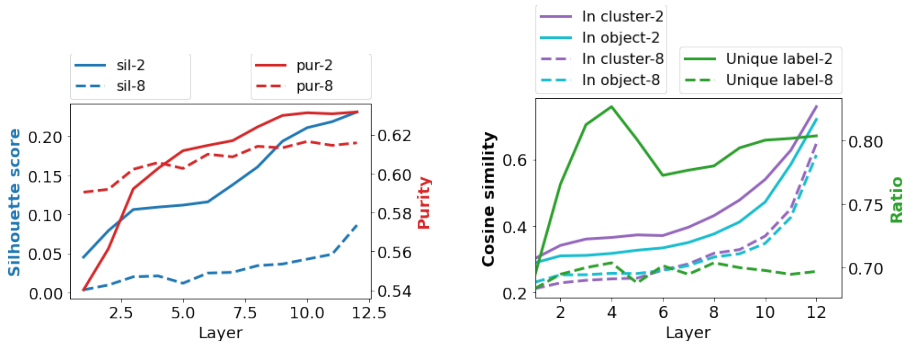


Figure 10: The visualization of the average the clustering measures for shuffling images. The purity and Silhouette scores for the  $2 \times 2$  shuffling are higher than for the  $8 \times 8$  shuffling, but they are all low. The in-cluster and in-object similarities are rather high for the  $2 \times 2$  shuffling, whereas they are much lower for the  $8 \times 8$  shuffling.

**Clustering behavior for shuffling images:** We investigate the clustering behavior for the patch-shuffling images. We first use t-SNE to visualize feature embeddings across the layers for patch-shuffling images, followed by the evaluation of the clustering measures for the real shuffling images. We observe that for the  $2 \times 2$  shuffling, all measures are rather good, meaning that ViT are quite robust to patch shuffling, whereas for the  $8 \times 8$  shuffling, all measures are significantly hurt.

To conclude, we notice that although in this work, we have not further exploited the clustering behavior of the feature embeddings in a real-world application, we believe this clustering behavior if strengthened properly using for example contrastive learning [5, 12] might possibly create more contrastive feature embeddings to benefit downstream tasks.

## **4 Conclusion**

In this paper, we propose a visualization technique to visually expose the information carried in a neuron or an embedding at a certain layer of ViTs. Our visualization technique helps to visualize the local and global information on an image represented by a neuron or a group of neurons. By observing and analyzing the visual outcome of our visualization technique, we come with some findings, wherein the most important one is the clustering behavior of the embeddings across the layers of ViTs. We establish the sketch mathematical explanation for this behavior as well as conducting experiments on real images to quantitatively verify it.

## References

- [1] Yutong Bai, Jieru Mei, Alan L Yuille, and Cihang Xie. Are transformers more robust than cnns? *Advances in Neural Information Processing Systems*, 34, 2021.
- [2] Srinadh Bhojanapalli, Ayan Chakrabarti, Daniel Glasner, Daliang Li, Thomas Unterthiner, and Andreas Veit. Understanding robustness of transformers for image classification. In *Proceedings of the IEEE/CVF International Conference on Computer Vision*, pages 10231–10241, 2021.
- [3] Nicolas Carion, Francisco Massa, Gabriel Synnaeve, Nicolas Usunier, Alexander Kirillov, and Sergey Zagoruyko. End-to-end object detection with transformers. In *European conference on computer vision*, pages 213–229. Springer, 2020.
- [4] Chun-Fu Richard Chen, Quanfu Fan, and Rameswar Panda. Crossvit: Cross-attention multi-scale vision transformer for image classification. In *Proceedings of the IEEE/CVF International Conference on Computer Vision*, pages 357–366, 2021.
- [5] Ting Chen, Simon Kornblith, Mohammad Norouzi, and Geoffrey Hinton. A simple framework for contrastive learning of visual representations. In *International conference on machine learning*, pages 1597–1607. PMLR, 2020.
- [6] Marcella Cornia, Matteo Stefanini, Lorenzo Baraldi, and Rita Cucchiara. Meshed-memory transformer for image captioning. In *Proceedings of the IEEE/CVF Conference on Computer Vision and Pattern Recognition*, pages 10578–10587, 2020.
- [7] Jia Deng, Wei Dong, Richard Socher, Li-Jia Li, Kai Li, and Li Fei-Fei. Imagenet: A large-scale hierarchical image database. In *2009 IEEE conference on computer vision and pattern recognition*, pages 248–255. Ieee, 2009.
- [8] Jacob Devlin, Ming-Wei Chang, Kenton Lee, and Kristina Toutanova. Bert: Pre-training of deep bidirectional transformers for language understanding. *arXiv preprint arXiv:1810.04805*, 2018.
- [9] Alexey Dosovitskiy, Lucas Beyer, Alexander Kolesnikov, Dirk Weissenborn, Xiaohua Zhai, Thomas Unterthiner, Mostafa Dehghani, Matthias Minderer, Georg Heigold, Sylvain Gelly, Jakob Uszkoreit, and Neil Houlsby. An image is worth 16x16 words: Transformers for image recognition at scale. In *International Conference on Learning Representations*, 2021.
- [10] M. Everingham, L. Van Gool, C. K. I. Williams, J. Winn, and A. Zisserman. The pascal visual object classes (voc) challenge. *International Journal of Computer Vision*, 88(2):303–338, June 2010.
- [11] Kaiming He, Xiangyu Zhang, Shaoqing Ren, and Jian Sun. Deep residual learning for image recognition. In *Proceedings of the IEEE conference on computer vision and pattern recognition*, pages 770–778, 2016.
- [12] Prannay Khosla, Piotr Teterwak, Chen Wang, Aaron Sarna, Yonglong Tian, Phillip Isola, Aaron Maschiot, Ce Liu, and Dilip Krishnan. Supervised contrastive learning. *Advances in Neural Information Processing Systems*, 33:18661–18673, 2020.
- [13] Yann LeCun, Yoshua Bengio, et al. Convolutional networks for images, speech, and time series. *The handbook of brain theory and neural networks*, 3361(10):1995, 1995.
- [14] Shilong Liu, Feng Li, Hao Zhang, Xiao Yang, Xianbiao Qi, Hang Su, Jun Zhu, and Lei Zhang. Dab-detr: Dynamic anchor boxes are better queries for detr. *arXiv preprint arXiv:2201.12329*, 2022.
- [15] David Martin, Charless Fowlkes, Doron Tal, and Jitendra Malik. A database of human segmented natural images and its application to evaluating segmentation algorithms and measuring ecological statistics. In *Proceedings Eighth IEEE International Conference on Computer Vision. ICCV 2001*, volume 2, pages 416–423. IEEE, 2001.
- [16] Kevin P. Murphy. *Probabilistic Machine Learning: An introduction*. MIT Press, 2022.
- [17] Muzammal Naseer, Kanchana Ranasinghe, Salman Khan, Munawar Hayat, Fahad Khan, and Ming-Hsuan Yang. Intriguing properties of vision transformers. In A. Beygelzimer, Y. Dauphin, P. Liang, and J. Wortman Vaughan, editors, *Advances in Neural Information Processing Systems*, 2021.
- [18] Namuk Park and Songkuk Kim. How do vision transformers work? *arXiv preprint arXiv:2202.06709*, 2022.

- [19] Maithra Raghu, Thomas Unterthiner, Simon Kornblith, Chiyuan Zhang, and Alexey Dosovitskiy. Do vision transformers see like convolutional neural networks? *Advances in Neural Information Processing Systems*, 34, 2021.
- [20] Olga Russakovsky, Jia Deng, Hao Su, Jonathan Krause, Sanjeev Satheesh, Sean Ma, Zhiheng Huang, Andrej Karpathy, Aditya Khosla, Michael Bernstein, et al. Imagenet large scale visual recognition challenge. *International journal of computer vision*, 115(3):211–252, 2015.
- [21] Ketan Rajshekhar Shahapure and Charles Nicholas. Cluster quality analysis using silhouette score. In *2020 IEEE 7th International Conference on Data Science and Advanced Analytics (DSAA)*, pages 747–748, 2020.
- [22] Rulin Shao, Zhouxing Shi, Jinfeng Yi, Pin-Yu Chen, and Cho-Jui Hsieh. On the adversarial robustness of visual transformers. *arXiv e-prints*, pages arXiv–2103, 2021.
- [23] Robin Strudel, Ricardo Garcia, Ivan Laptev, and Cordelia Schmid. Segformer: Transformer for semantic segmentation. In *Proceedings of the IEEE/CVF International Conference on Computer Vision*, pages 7262–7272, 2021.
- [24] Mingxing Tan and Quoc Le. Efficientnet: Rethinking model scaling for convolutional neural networks. In *International conference on machine learning*, pages 6105–6114. PMLR, 2019.
- [25] Hugo Touvron, Matthieu Cord, Matthijs Douze, Francisco Massa, Alexandre Sablayrolles, and Herve Jegou. Training data-efficient image transformers & distillation through attention. In Marina Meila and Tong Zhang, editors, *Proceedings of the 38th International Conference on Machine Learning*, volume 139 of *Proceedings of Machine Learning Research*, pages 10347–10357. PMLR, 18–24 Jul 2021.
- [26] Laurens van der Maaten and Geoffrey Hinton. Visualizing data using t-sne. *Journal of Machine Learning Research*, 9(86):2579–2605, 2008.
- [27] Ashish Vaswani, Noam Shazeer, Niki Parmar, Jakob Uszkoreit, Llion Jones, Aidan N Gomez, Łukasz Kaiser, and Illia Polosukhin. Attention is all you need. In *Advances in Neural Information Processing Systems*, volume 30. Curran Associates, Inc., 2017.
- [28] Ashish Vaswani, Noam Shazeer, Niki Parmar, Jakob Uszkoreit, Llion Jones, Aidan N Gomez, Łukasz Kaiser, and Illia Polosukhin. Attention is all you need. *Advances in neural information processing systems*, 30, 2017.
- [29] Enze Xie, Wenhai Wang, Zhiding Yu, Anima Anandkumar, Jose M Alvarez, and Ping Luo. Segformer: Simple and efficient design for semantic segmentation with transformers. *Advances in Neural Information Processing Systems*, 34, 2021.
- [30] Jun Yu, Jing Li, Zhou Yu, and Qingming Huang. Multimodal transformer with multi-view visual representation for image captioning. *IEEE transactions on circuits and systems for video technology*, 30(12):4467–4480, 2019.
- [31] Sixiao Zheng, Jiachen Lu, Hengshuang Zhao, Xiatian Zhu, Zekun Luo, Yabiao Wang, Yanwei Fu, Jianfeng Feng, Tao Xiang, Philip HS Torr, et al. Rethinking semantic segmentation from a sequence-to-sequence perspective with transformers. In *Proceedings of the IEEE/CVF conference on computer vision and pattern recognition*, pages 6881–6890, 2021.
- [32] Xizhou Zhu, Weijie Su, Lewei Lu, Bin Li, Xiaogang Wang, and Jifeng Dai. Deformable detr: Deformable transformers for end-to-end object detection. *arXiv preprint arXiv:2010.04159*, 2020.

## Appendix

### A Theoretical Development

**Mathematical explanation for the clustering behavior:** We consider the single-head self-attention with the key matrix  $W_K$ , the query matrix  $W_Q$ , and the value matrix  $W_V$ . We examine the embeddings at two consecutive layers:  $\mathbf{z}_t \in \mathbb{R}^{(N+1) \times D}$  and  $\mathbf{z}_{t+1} \in \mathbb{R}^{(N+1) \times D}$ , where each row of them is an embedding. The attention weights  $\mathbf{a}_t^{k,j}$  are computed based on the similarity of the linear projections of  $\mathbf{z}_t^k$  and  $\mathbf{z}_t^j$  w.r.t.  $W_K$  and  $W_Q$  respectively. We then apply the linear projection to  $\mathbf{z}_t^j$ ,  $j = 0, \dots, N$ , then compute  $\tilde{\mathbf{z}}_{t+1}^j$ ,  $j = 0, \dots, N$ , and finally do another linear projection to project  $\tilde{\mathbf{z}}_{t+1}^j$ ,  $j = 0, \dots, N$

back to the embedding space to obtain  $\mathbf{z}_{t+1}^j, j = 0, \dots, N$ . To simplify our analysis, we further assume that  $W_V = \mathbb{I}$  (i.e., the identity matrix). Therefore, we compute the embeddings in the next layer as  $\mathbf{z}_{t+1}^j = \sum_{k=0}^N \mathbf{a}_t^{k,j} \mathbf{z}_t^k$ . We develop the following theorem regarding the clustering behavior of the embeddings.

**Theorem A.1.** *Let  $d(A) = \max_{\mathbf{a}, \mathbf{b} \in A} \|\mathbf{a} - \mathbf{b}\|_2$  be the diameter of the set  $A$ . The following statements hold*

i)  $d(Z_{t+1}) \leq d(Z_t)$ , where  $Z_t$  and  $Z_{t+1}$  are the sets of the row vectors (i.e., the embeddings) of  $\mathbf{z}_t$  and  $\mathbf{z}_{t+1}$  respectively.

ii) Assume that the embeddings  $Z_t$  (or  $\mathbf{z}_t$ ) can be grouped into  $M$  clusters  $Z_t^m = \{\mathbf{z}_t^j : j \in G^m\}$ , where  $[G^m]_{m=1}^M$  is a partition of  $\{0, 1, \dots, N\}$  such that if  $j \in G^m$  and  $j' \in G^{m'}$  with  $m \neq m'$ , the attention weight  $\epsilon_l < \mathbf{a}_t^{j',j} < \epsilon_u$  for  $\epsilon_u \geq \epsilon_l \geq 0$ . This condition means that if  $\mathbf{z}_t^j$  and  $\mathbf{z}_t^{j'}$  belong to two different clusters, they are less similar and their attention weight  $\mathbf{a}_t^{j',j}$  is possibly small. Let  $N_m = |G^m|$  be the cardinality of the cluster  $m$ . For any  $m$ , we have the following inequality:

$$d(Z_{t+1}^m) < (1 - A_m \epsilon_l)^2 d(Z_t^m) + A_m \epsilon_u d(Z_t) (A_m \epsilon_u + 2), \quad (2)$$

where  $A_m = N + 1 - N_m$  and  $Z_{t+1}^m = \{\mathbf{z}_{t+1}^i : i \in G^m\}$  is the cluster in the next layer. Note that  $d(Z_{t+1}^m)$  and  $d(Z_t^m)$  are exactly the intra-cluster distances for these clusters.

### Proof of Theorem 3.1.

i) Because the distance  $h(\mathbf{a}, \mathbf{b}) = \|\mathbf{a} - \mathbf{b}\|_2$  is a convex function, we have

$$\begin{aligned} \left\| \mathbf{z}_t^j - \mathbf{z}_t^{j'} \right\|_2 &= \left\| \sum_{k=0}^N \mathbf{a}_t^{k,j} \mathbf{z}_t^k - \sum_{k=0}^N \mathbf{a}_t^{k,j'} \mathbf{z}_t^k \right\|_2 = h \left( \sum_{k=0}^N \mathbf{a}_t^{k,j} \mathbf{z}_t^k, \sum_{k=0}^N \mathbf{a}_t^{k,j'} \mathbf{z}_t^k \right) \\ &\leq \sum_{k=0}^N \sum_{k'=0}^N \mathbf{a}_t^{k,j} \mathbf{a}_t^{k',j'} h(\mathbf{z}_t^k, \mathbf{z}_t^{k'}) \leq \sum_{k=0}^N \sum_{k'=0}^N \mathbf{a}_t^{k,j} \mathbf{a}_t^{k',j'} d(Z_t) \\ &= \sum_{k=0}^N \mathbf{a}_t^{k,j} \sum_{k'=0}^N \mathbf{a}_t^{k',j'} d(Z_t) = d(Z_t). \end{aligned}$$

Therefore, we reach  $d(Z_{t+1}) \leq d(Z_t)$ .

ii) For any  $j, j' \in G^m$ , we derive as

$$\begin{aligned} \left\| \mathbf{z}_t^j - \mathbf{z}_t^{j'} \right\|_2 &= \left\| \sum_{k=0}^N \mathbf{a}_t^{k,j} \mathbf{z}_t^k - \sum_{k=0}^N \mathbf{a}_t^{k,j'} \mathbf{z}_t^k \right\|_2 = h \left( \sum_{k=0}^N \mathbf{a}_t^{k,j} \mathbf{z}_t^k, \sum_{k=0}^N \mathbf{a}_t^{k,j'} \mathbf{z}_t^k \right) \\ &\leq \sum_{k=0}^N \sum_{k'=0}^N \mathbf{a}_t^{k,j} \mathbf{a}_t^{k',j'} h(\mathbf{z}_t^k, \mathbf{z}_t^{k'}) \\ &\leq \sum_{k \in G^m} \sum_{k' \in G^m} \mathbf{a}_t^{k,j} \mathbf{a}_t^{k',j'} h(\mathbf{z}_t^k, \mathbf{z}_t^{k'}) + \sum_{k \in G^m} \sum_{k' \notin G^m} \mathbf{a}_t^{k,j} \mathbf{a}_t^{k',j'} h(\mathbf{z}_t^k, \mathbf{z}_t^{k'}) \\ &+ \sum_{k \notin G^m} \sum_{k' \in G^m} \mathbf{a}_t^{k,j} \mathbf{a}_t^{k',j'} h(\mathbf{z}_t^k, \mathbf{z}_t^{k'}) + \sum_{k \notin G^m} \sum_{k' \notin G^m} \mathbf{a}_t^{k,j} \mathbf{a}_t^{k',j'} h(\mathbf{z}_t^k, \mathbf{z}_t^{k'}) \\ &\leq \sum_{k \in G^m} \sum_{k' \in G^m} \mathbf{a}_t^{k,j} \mathbf{a}_t^{k',j'} d(Z_t^m) + \sum_{k \in G^m} \sum_{k' \notin G^m} \mathbf{a}_t^{k,j} \mathbf{a}_t^{k',j'} d(Z_t) \\ &+ \sum_{k \notin G^m} \sum_{k' \in G^m} \mathbf{a}_t^{k,j} \mathbf{a}_t^{k',j'} d(Z_t) + \sum_{k \notin G^m} \sum_{k' \notin G^m} \mathbf{a}_t^{k,j} \mathbf{a}_t^{k',j'} d(Z_t). \end{aligned}$$

We further manipulate as

$$\begin{aligned} \sum_{k \in G^m} \sum_{k' \in G^m} \mathbf{a}_t^{k,j} \mathbf{a}_t^{k',j'} d(Z_t^m) &= d(Z_t^m) \sum_{k \in G^m} \mathbf{a}_t^{k,j} \sum_{k' \in G^m} \mathbf{a}_t^{k',j'} \\ &= d(Z_t^m) \left( 1 - \sum_{k \notin G^m} \mathbf{a}_t^{k,j} \right) \left( 1 - \sum_{k' \notin G^m} \mathbf{a}_t^{k',j'} \right) \\ &< d(Z_t^m) (1 - A_m \epsilon_l)^2 d(Z_t^m). \end{aligned}$$

$$\begin{aligned} \sum_{k \in G^m} \sum_{k' \notin G^m} \mathbf{a}_t^{k,j} \mathbf{a}_t^{k',j'} d(Z_t) &= d(Z_t) \sum_{k \in G^m} \mathbf{a}_t^{k,j} \sum_{k' \notin G^m} \mathbf{a}_t^{k',j'} \\ &< A_m \epsilon_u d(Z_t). \end{aligned}$$

$$\begin{aligned} \sum_{k \notin G^m} \sum_{k' \in G^m} \mathbf{a}_t^{k,j} \mathbf{a}_t^{k',j'} d(Z_t) &= d(Z_t) \sum_{k \notin G^m} \mathbf{a}_t^{k,j} \sum_{k' \in G^m} \mathbf{a}_t^{k',j'} \\ &< A_m \epsilon_u d(Z_t). \end{aligned}$$

$$\begin{aligned} \sum_{k \notin G^m} \sum_{k' \notin G^m} \mathbf{a}_t^{k,j} \mathbf{a}_t^{k',j'} d(Z_t) &= d(Z_t) \sum_{k \notin G^m} \mathbf{a}_t^{k,j} \sum_{k' \notin G^m} \mathbf{a}_t^{k',j'} \\ &< A_m^2 \epsilon_u^2 d(Z_t). \end{aligned}$$

Finally, we arrive at

$$\left\| \mathbf{z}_t^j - \mathbf{z}_t^{j'} \right\|_2^2 < (1 - A_m \epsilon_l)^2 d(Z_t^m) + A_m \epsilon_u d(Z_t) (A_m \epsilon_u + 2).$$

$$d(Z_{t+1}^m) < (1 - A_m \epsilon_l)^2 d(Z_t^m) + A_m \epsilon_u d(Z_t) (A_m \epsilon_u + 2).$$

It is worth noting that our proof can be generalized to any convex distances, e.g.,  $h(\mathbf{a}, \mathbf{b}) = \|\mathbf{a} - \mathbf{b}\|_p$  ( $p \geq 1$ ). We made a minor typo in Inequality (1) in the main paper. We will correct it in the revised version. Sorry for this inconvenience.

## B Neural behavior for image occlusion

### B.1 Clustering Metrics

**Purity score [16]:** Given a cluster  $Z_t^m$ , we define  $p_m = \max_i p_{mi}$  as the frequency of the most dominated labels (e.g., object types or background) and compute the purity as:

$$\text{purity} = \sum_{m=1}^M p_m \frac{N_m}{N+1}.$$

A *high purity* means that each cluster is more pure or mostly dominated by a label.

**Silhouette score [21]:** For each  $\mathbf{z}_t^j \in Z_t^m$ , we compute the corresponding intra-distance and inter-distance as

$$\begin{aligned} a(\mathbf{z}_t^j) &= \frac{1}{|N_m| - 1} \sum_{j' \in G^m, j' \neq j} \left\| \mathbf{z}_t^j - \mathbf{z}_t^{j'} \right\|_2. \\ b(\mathbf{z}_t^j) &= \min_{m' \neq m} \frac{1}{|N_{m'}|} \sum_{j' \in G^{m'}} \left\| \mathbf{z}_t^j - \mathbf{z}_t^{j'} \right\|_2. \end{aligned}$$

The Silhouette score at  $\mathbf{z}_t^j \in Z_t^m$  is computed as

$$\text{Silhouette}(\mathbf{z}_t^j) = \frac{b(\mathbf{z}_t^j) - a(\mathbf{z}_t^j)}{\max\{a(\mathbf{z}_t^j), b(\mathbf{z}_t^j)\}},$$

and the Silhouette score is the average of the Silhouette scores at the embeddings.

A *high Silhouette* score implies the intra-cluster distances are relatively smaller than the inter-cluster distances.

**Unique label ratio:** This is measured as the ratio of the number of unique dominated object-type labels and the number of unique object-type labels. A *high unique label ratio* implies that for most of object-type label, there exists at least a cluster dominated by this object-type label.

We investigate the clustering behavior for image occlusion. In which, we apply three types of occlusion: *Random drop*, *salient* and *non-salient* occlusion, with different ratios (from 0.2 to 0.8 for random drop and salient occlusion, from 0.2 to 1.0 for non-salient occlusion). Note that the number of data for each setting is different because we select only images with at least two big objects as described in Section 3.2. Additionally, patches in the images are dropped randomly, therefore, possibly reducing the number of tokens for each object in the image. This process is mentioned in detail below.

## B.2 Random drop

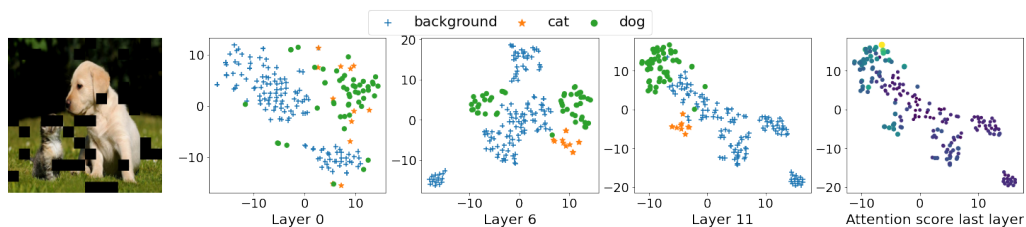
We randomly choose  $k$  patches in each image to change pixels to 0, called un-informative patches, with  $k = n * r$ ,  $n$  is the total number of patch in the image and  $r \in \{0.2, 0.4, 0.6, 0.8\}$ . When  $r$  increases, the number of informative patches decreases as same as the number of object tokens. As mentioned in Section 3.2 in the main paper, we select the images with at least two big objects to investigate the clustering behavior, so that the number of data matching the requirement decreases when  $r$  increases. Particularly, there are 494, 438, 337, 177 valid images for corresponding  $r$ . A sample for each value of  $r$  is displayed in Figure 11 along with its t-SNE of feature embeddings. It can be observed that with  $r = \{0.2, 0.4, 0.6\}$ , ViT is still able to group the object tokens into clusters at higher layers. But increasing  $r$  to 0.8, ViT barely distinguishes the object and non-object tokens. However, in all settings of  $r$ , the feature embeddings belonging to the same object still stay closer together and the attention weights for object-patch embeddings are also higher than the others.

Figure 12 compares the clustering measures of random drop at different ratios. In general, all scores decrease when  $r$  increases but they all increase across layers. This demonstrates the ability of ViTs to group embeddings of the same objects and find the correct object patches to pay attention to. The purity and unique label ratio drop across values of  $r$  shows ViTs could be noise by background when losing significant number of informative patches. Mean that ViTs find it harder to distinguish background and foreground if the information is not enough.

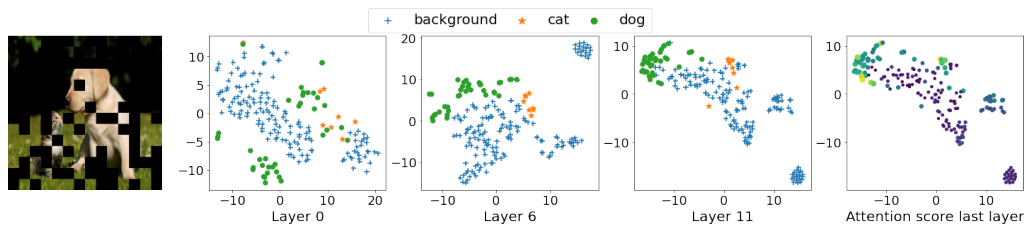
## B.3 Salient occlusion

Instead of randomly choosing a part of all patches in an image, the salient occlusion only drops some object patches, depending on ratio  $r$ . So that, even with the same value of  $r$ , the number of valid images is different between random drop and salient occlusion. Particularly, 494, 441, 355, 194 valid images for  $r \in \{0.2, 0.4, 0.6, 0.8\}$  respectively. A sample for each value of  $r$  is presented in Figure 12. The behavior of feature embeddings is also similar to random drop occlusion that increasing  $r$ , ViTs find it harder to distinguish object and non-object embeddings but the cosine similarity of object embeddings are higher across layers.

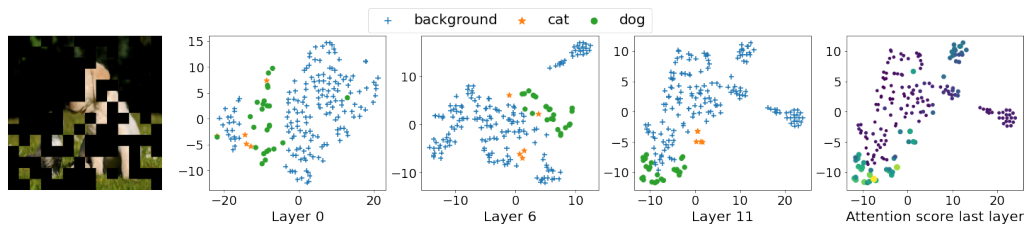
Figure 13 shows the clustering score for ViT when apply the salient occlusion process. The purity score is the most significant change along the increase of  $r$ . Means that it gets harder to separate embeddings of different objects when gradually losing object detail (object patches). Together with the modest change of the unique label ratio across values of  $r$  show ViTs may learn to separate objects in different categories (i.e. object cat and object dog) better than in the same categories (i.e. two object cats).



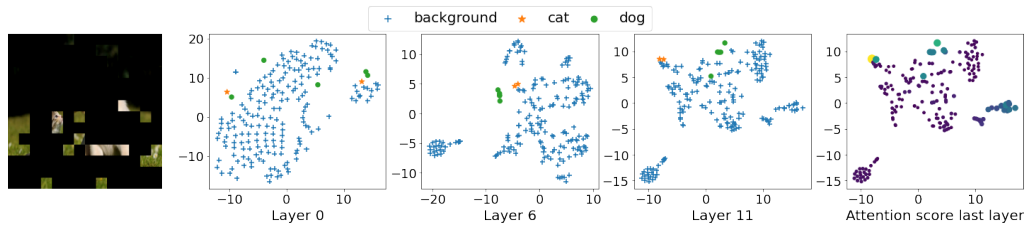
(a) Random drop at ratio 0.2.



(b) Random drop at ratio 0.4.



(c) Random drop at ratio 0.6.



(d) Random drop at ratio 0.8.

Figure 11: t-SNE of feature embeddings across the layers of ViT. The Pascal VOC dataset is processed with random drop at different ratio from 0.2 to 0.8

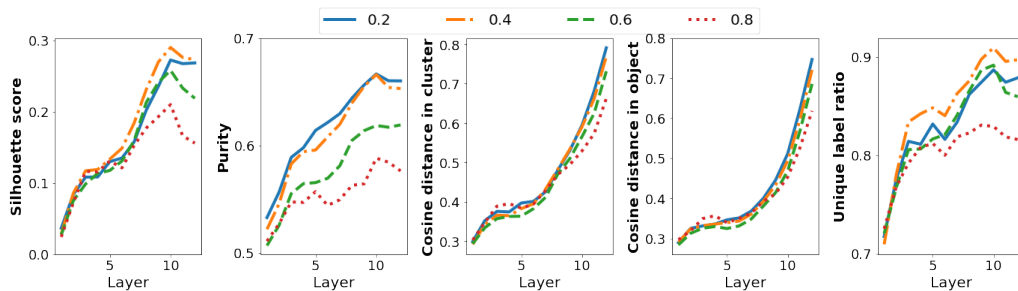
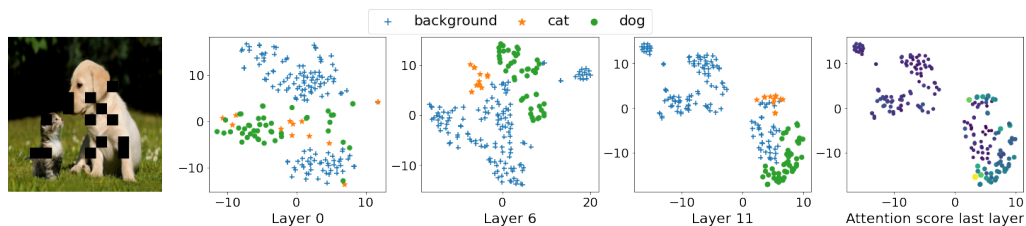
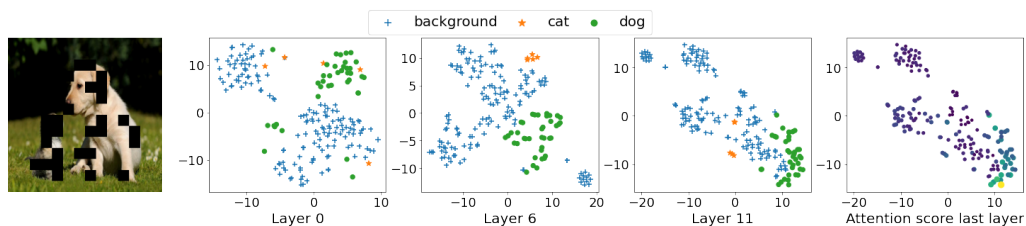


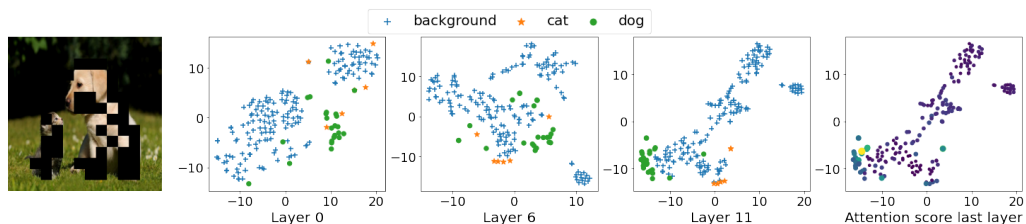
Figure 12: Clustering measurement of embeddings with **random drop**. The images in Pascal VOC dataset are processed with random dropping at different ratio from 0.2 to 0.8. With higher ratio of occlusion, the ViTs is getting harder to distinguish object to object and also object to non-object



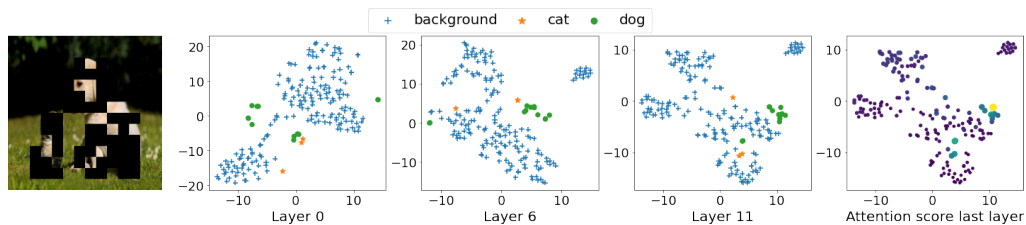
(a) Salient occlusion at ratio 0.2.



(b) Salient occlusion at ratio 0.4.



(c) Salient occlusion at ratio 0.6.



(d) Salient occlusion at ratio 0.8.

Figure 12: t-SNE of feature embeddings across the layers of ViT. The Pascal VOC dataset is processed with salient occlusion at different ratio from 0.2 to 0.8

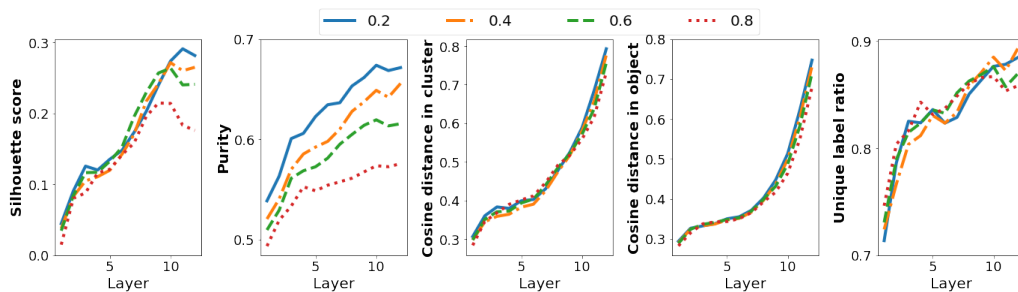
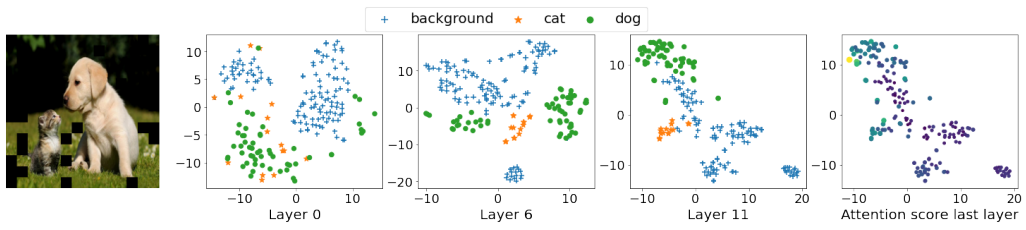
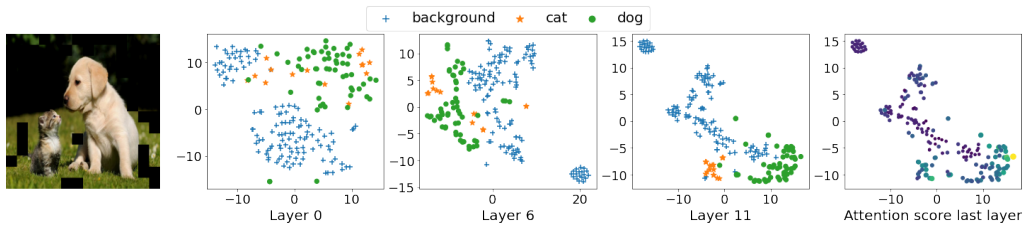


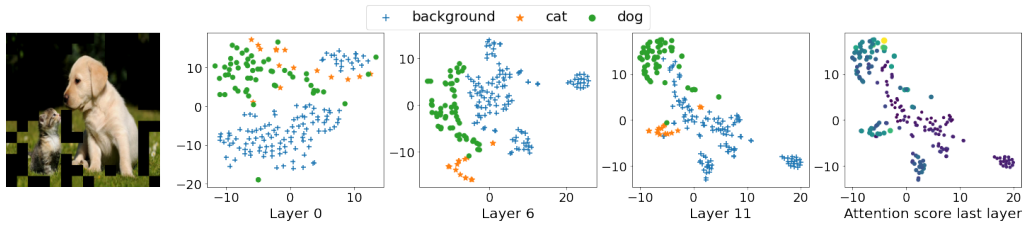
Figure 13: Clustering measurement of embeddings with **salient occlusion**. The images in Pascal VOC dataset are processed with salient occlusion at different ratio from 0.2 to 0.8. With higher ratio of occlusion, embeddings in cluster or of an object still preserve the high similarity but ViTs find it harder to distinguish object to object.



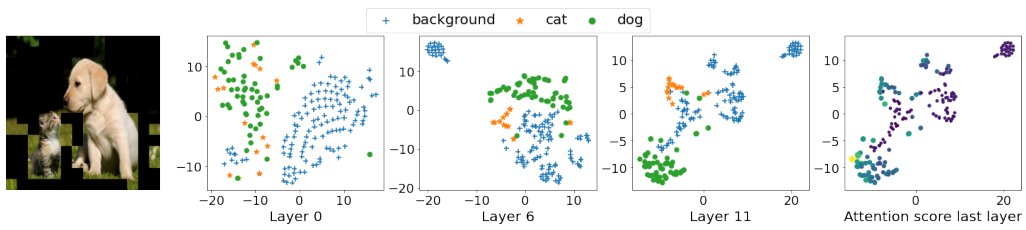
(a) Non-salient occlusion at ratio 0.2.



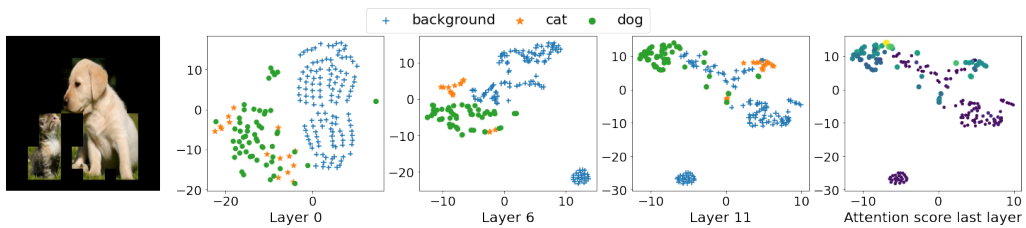
(b) Non-salient occlusion at ratio 0.4.



(c) Non-salient occlusion at ratio 0.6.



(d) Non-salient occlusion at ratio 0.8.



(e) Non-salient occlusion at ratio 1.0.

Figure 14: t-SNE of feature embeddings across the layers of ViT. The Pascal VOC dataset is processed with **non-salient occlusion** at different ratio from 0.2 to 0.8

## B.4 Non-salient occlusion

The pre-process is the same as salient occlusion but choosing the non-object patches to drop. As mentioned above, we select the images with big objects so that the non-salient occlusion does not impact to number of valid data, which is the same 530 images for all value of  $r$ . Samples for different ratios are presented in Figure 14 while the clustering measures in presented in Figure 15. Apparently, increasing  $r$  helps remove background noise, therefore, ViTs could group object embeddings clearly in the very first layer. It also shows this phenomenon in unique label ratio plot since more objects are formed in clusters increasing ratio  $r$ . The other cluster measures in Figure 15 shows a small change. In general, removing background makes ViTs more focus on distinguish objects and object embeddings less attractive by non-object ones.

Interestingly, as presented in Figure 14e, non-object embeddings are formed in one cluster in very first layers (as the value of these patches is all zeros). However, in higher layers (e.g., 6th and 11th layers), we clearly see two clusters of embeddings corresponding to non-salient patches. We reason that the position of patches affects to embedding across ViT’s layers. When non-salient patches are set to zero, the positional encodings are the only factor impact the attention scores, so that the attention scores to object-patches might be higher for non-salient patches, which are close to object-patches. As a result, the embeddings corresponding to non-salient patches, which are close to object-patches, might gather more information in comparison with the ones that are far way from object-patches, leading to two separate clusters in higher layers (as discussion in Section 3.1.2 in the main paper, the visualization of higher layer linearly aggregates information from lower layer weighted by attention score). To confirm this observation, we change value of non-salient patches to random noise instead of zero, which would reduce the impact of positional encoding when calculating attention map. It can be seen from Figure 16 that tokens corresponding to non-salient patches are well grouped in only one cluster.

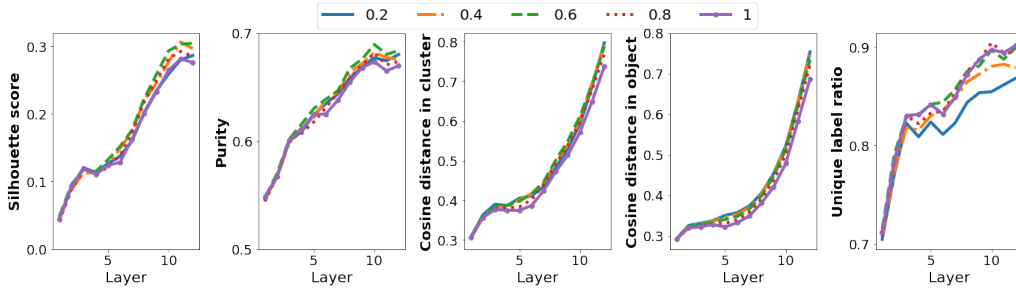


Figure 15: Clustering measurement of embeddings with **non-salient occlusion**. The images in Pascal VOC dataset are processed with non-salient occlusion at different ratio from 0.2 to 0.8.

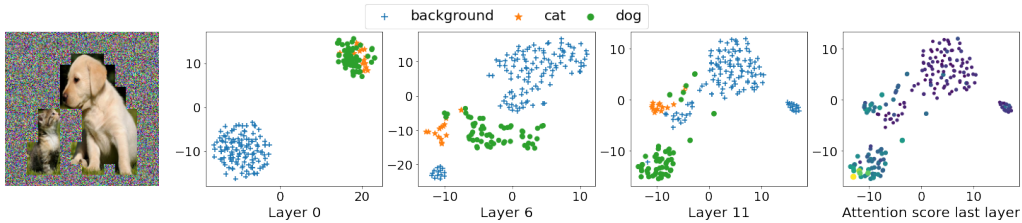


Figure 16: A sample of feature embeddings when replacing all pixels in non-object patches with random noise (instead of changing to 0 like non-salient occlusion)